



# Annealing recovery of nanoscale silicon surface damage caused by Ga focused ion beam



Y.J. Xiao, F.Z. Fang\*, Z.W. Xu\*\*, X.T. Hu

State Key Laboratory of Precision Measuring Technology & Instruments, Centre of MicroNano Manufacturing Technology, Tianjin University, 300072, China

## ARTICLE INFO

### Article history:

Received 21 December 2014

Received in revised form 13 February 2015

Accepted 11 March 2015

Available online 19 March 2015

### Keywords:

Focused ion beam (FIB)

Annealing

Silicon

Gallium

Molecular dynamics (MD)

## ABSTRACT

In this paper, molecular dynamics method with the Tersoff–ZBL combined interatomic potential was adopted to study the dynamics of focused ion beam (FIB) milling and subsequent annealing. The Ga FIB induced damage and its recovery mechanism during subsequent annealing process were investigated in nanoscale time and space. To investigate the nanoscale damage during FIB milling with the ion energy of 0.5 keV, 1 keV and 2 keV, radial distribution function, bond length distribution, bond angle distribution, and common neighbour analysis (CNA) were calculated and analyzed under various ion doses. FIB irradiated silicon substrate with ion dose of  $2 \times 10^{14}$  ions/cm<sup>2</sup> was annealed at various annealing temperatures from 1400 K to 2400 K. Molecular dynamics simulation illustrated that as *a*-Si region was surrounded by *c*-Si after implantation, the recrystallization lead to a *c*-Si regrowth processes both from bottom towards top surface and from periphery to centre. The damage area profiles by CNA represented a shortest recovery time of 2.0 ns at 2200 K. Both melting on the top surface and recrystallization at crystalline/amorphous interface have existed as annealing at 2400 K, which is near the melting point. Ga migrated together and moved towards the surface with the *a*-Si/*c*-Si interface.

© 2015 Elsevier B.V. All rights reserved.

## 1. Introduction

With a trend of increasing miniaturization of devices and components in recent year, focused ion beam (FIB) has become an indispensable tools for abundant applications in the field of micro/nano-manufacture, including transmission electron microscopy (TEM) sample preparation [1,2], semiconductor devices failure analysis [3], 3-dimensional structure [4], patterning [5,6] and surface characterization or secondary electron imaging [7,8]. The major developments of FIB instrument used liquid metal ion source (LIMS) were during the late 1970s and the early 1980s, since the first high brightness gallium (Ga) LIMS had been invented by Krohn and Ringo from American National Laboratory Argonne in 1975 [9]. Until now, the Ga LIMS is still widely available profit from its low melting point (29.8 °C) [10], low vapour pressure (<10–12 Torr) and excellent oxidation stability [11].

It is unable to avoid the formation of amorphous layers during FIB milling. As the ion dose increases, the ion collisions can cause

point-like damage, defect clusters, amorphous pockets; and finally form continuous amorphous layers [12]. The ion-implanted impurity (Ga<sup>+</sup> ions) can also form a contamination layer on the target [13]. The alternation of surface micro-structure and chemical composition would degrade the optical [14–16], electrical [17,18] and mechanical [19] properties of devices. The TEM resolution is also reduced by the damage layers on the two faces of TEM samples [20].

To study the dynamics of solids processing by energetic particles, molecular dynamics (MD) simulation based on empirical potential has been employed in recent decades. Caturla et al. employed molecular dynamics to study cascades of different ion mass and energy in silicon after single-ion implanted [21]. Krasheninnikov et al. built molecular dynamics moulds of ion impacts on nanotubes to investigate the formation of ion-irradiation-induced defects [22]. The processes of clusters and molecular implantation to silicon have also been investigated using molecular dynamics simulations [23,24]. A few MD calculations are focused on the interactions between focused ion beams especial Ga<sup>+</sup> ions and target atoms. Russo et al. performed MD simulations of Ga<sup>+</sup> FIB-milling with 2 keV and 30 keV energies to examine the extent of lateral damage, sputtering and displacement of target atoms [25]. Pastewka et al. calculated surface amorphization, sputter rate, and intrinsic stresses of silicon during FIB [26].

In order to remove the strain and recrystallize the amorphous pockets, some researchers have tried a post repair process, i.e.,

\* Corresponding author at: Building 5, No. 108, Tianjin University, 92 Weijin Road, Nankai District, Tianjin 300072, China. Tel.: +86 22 27407503; fax: +86 22 59813864.

\*\* Corresponding author at: Building 5, No. 108, Tianjin University, 92 Weijin Road, Nankai District, Tianjin 300072, China. Tel.: +86 022 27403753.

E-mail addresses: [fzfang@gmail.com](mailto:fzfang@gmail.com) (F.Z. Fang), [zongweixu@163.com](mailto:zongweixu@163.com) (Z.W. Xu).

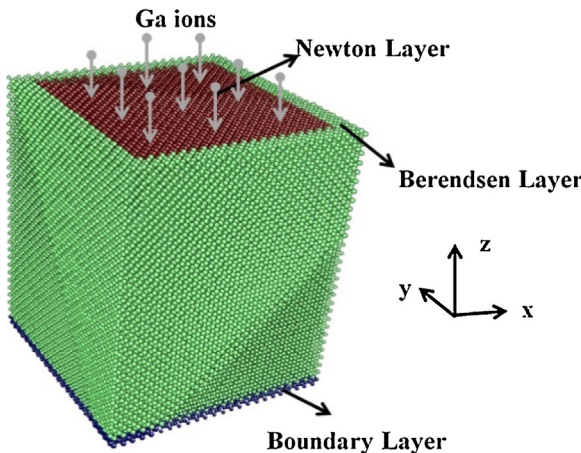


**Fig. 1.** The MD simulation mould for FIB milling.

annealing to limit these influences [15,18,27]. The transmission performance and optical quality of micro or nano-photonic devices, which is declined significantly being induced in silicon by etching with a focused-ion beam [14,15], improved after subsequent annealing [15]. Noise of FIB milled device significantly reduced after a low temperature annealing (200–600 °C) and cross phase shifts also increased [18,28].

Crystalline silicon (*c*-Si) has been chosen to investigate the system due to its contribution in the semiconductor and MEMS industry. In our previous work [29], the evolution of Si surface after FIB milling and subsequent annealing is studied. Gallium migrated to clusters in the top of amorphous Si (*a*-Si) layer, which was transformed from *c*-Si after large dose implantation. Ga impurity was completely segregated from Si after an annealing at 800 °C for 30 min, but the Si surface was left quite rough. Recently, array holes fabricated by the implantation of Ga ions were used to control quantum dot nucleation at >500 °C [30–32].

Fundamental researches on focused ion beam (FIB) induced damage play an important role in FIB nano-manufacturing and its application. However, either conducting actual experiments or characterizing sample performance at the nanoscale is a rather difficult task. Due to lack of online testing approaches in FIB machining, available experimental studies acquire rather fragmentary data. In consequence of this, MD simulation is chosen to obtain in-depth studies of the Ga<sup>+</sup> ions and materials the dynamics during FIB-milling and subsequent annealing in this paper. In this paper, the evolution of a hole formed by implantation in subsequent annealing is studied. Besides the ion implantation damage and recrystallization of Si, we have focused on the diffusion and movement of gallium during implantation and annealing in this study.

## 2. Computational details

### 2.1. MD mould for ion implantation

**Fig. 1** shows the 3D molecular dynamics simulation mould for Ga<sup>+</sup> focused ion beam milling. The target material is monocrystalline silicon with a size of 13 nm × 13 nm × 16.3 nm, including 138,240 Si atoms. The implantation area for a hole is 10 nm × 10 nm. The main atoms interacting with Ga<sup>+</sup> ions, which lay in the middle of the simulation box, belonged to the Newton layer. Their motion obeyed the classical Newton's second law. The Berendsen layer performed a Berendsen thermostat [33], and it would keep at a constant temperature of 293 K to imitate the heat dissipation. It contains several layers of atoms around the Newton layer except

the top side. Atoms at the bottom Si (0 0 1) plane were frozen during the whole process of ion implanted, for the purpose of imitating the boundary of Si, which supplied the simple avoidance of the translation of the simulation box along the ions implanting direction. The top-most Si (0 0 1) plane was free, i.e., the sputtered particles were removed from the system when they crossed the top of the simulation box. The [1 0 0] and [0 1 0] direction were applied periodic boundary conditions for an infinite plate.

The simulation started from an perfect initial slab of *c*-Si. Firstly, the system was equilibrated at 293 K for 50,000 iterations after initiated by assigning a Boltzmann distribution of velocities at 293 K. Then, a total of 200 Ga ions implanted to the silicon (0 0 1) one by one with the incident angle of 0°, which is perpendicular to the surface of Si. To study the influence of ion energy, the Si was impacted by Ga ions with the energy of 0.5 keV, 1 keV and 2 keV, respectively. The ions implanted to Si with a height of 1 nm above the bottom. The initial potential energy of Ga<sup>+</sup> is ignored, thus the initial kinetic energy of Ga ions is corresponding to the implantation energy. During the cascades in silicon atoms, the velocity of Ga ions greatly changes from 7.44 Å/fs (when the ion energy equal to 2 keV) to less than 0.02 Å/fs. Taking into account the computational limitations and simulation accuracy, the MD time-step was reset in a range of 0.002–1 fs during calculation, making sure no atom moves further than 0.02 Å per iteration [34]. The system was relaxed for 50,000 iterations after per Ga atom implanted, after which the whole slab would reach ~293 K. A Ga implanted rate of ~50 ps/ion, which decreases with the increasing of the initial ion energy, implies a flux of ~2 × 10<sup>22</sup> cm<sup>-2</sup> s<sup>-1</sup>. The molecular dynamics simulations were carried on LAMMPS programme code [35]. Structures were visualized using VMD (visual molecular dynamics) software [36] or AtomEye software [37].

The forces and energies in the system during ion collisions were briefly depicted by the empirical potential functions. A short range core repulsive ZBL potential [38] was used to describe the binary collision between Ga and Si at short inter-atomic distances. Considering the long range interactions among silicon atoms in the substrate for covalent systems, Tersoff potential [39] was splined smoothly to ZBL potential:

$$E = \frac{1}{2} \sum_i \sum_{j \neq i} V_{ij} \quad (1)$$

$$V_{ij} = (1 - f_F(r_{ij})) V_{ij}^{ZBL} + f_F(r_{ij}) V_{ij}^{Tersoff} \quad (2)$$

$$f_F(r_{ij}) = \frac{1}{1 + e^{-A_F(r_{ij}-r_c)}} \quad (3)$$

where the  $V_{ij}^{ZBL}$  and  $V_{ij}^{Tersoff}$  indicate ZBL portion and Tersoff portion, respectively. The parameters of  $A_F$  and  $r_c$  are used to adjust  $f_F$ :  $A_F$  controls how "sharp" the transition is between the ZBL portion and Tersoff portion, and  $r_c$  is essentially the cutoff for the ZBL potential.  $r_{ij}$  is equal to the distance between atoms  $i$  and  $j$ . The parameters of Tersoff potential for Si–Si and Ga–Ga interaction were given in Ref. [39] and Ref. [40], respectively.

### 2.2. MD simulation of annealing

After implantation with 200 Ga ions of 1 keV energy, the kinetics of the recrystallization process is studied. The system was annealed at different temperatures (1400 K, 1600 K, 1800 K, 2000 K, 2200 K and 2400 K) in vapour. Nose–Hoover thermostat (NPT ensemble) was used in the annealing system. Periodic boundary conditions were applied at all six faces. To save computational effort, the lower crystalline layer was removed before annealing, and only the upper amorphous layer with the thickness of 65.16 Å underwent thermal

**Table 1**  
Simulation parameters during implantation and crystallization.

Condition	Parameters
Work material	Slab of Si (0 0 1) plane
Lattice constant	$a_0 = 0.543 \text{ nm}$
Potential for Si–Si, Si–Ga, Ga–Ga	Tersoff-III & ZBL
Work dimensions during implantation	$24a_0 \times 24a_0 \times 30a_0$
Incident angle	0°
Bulk temperature	293 K
Ion energy	0.5 keV, 1 keV, 2 keV
Number of Ga ions	200
Implant area	$10 \text{ nm} \times 10 \text{ nm}$
Ion flux	$\sim 2 \times 10^{22} \text{ cm}^{-2} \text{ s}^{-1}$
Work dimensions during crystallization	$24a_0 \times 24a_0 \times 12a_0$
Annealing temperature	1400 K, 1800 K, 2000 K, 2200 K and 2400 K
Thermostat style	Nose–Hoover thermostat (NPT ensemble)

process. According to the Tersoff-ZBL potential, the surface melting point of monocrystalline silicon ( $T_{mc}$ ) is  $\sim 2550 \text{ K}$  [41,42], as the experimental value ( $T_{mc}^*$ ) is  $1681 \text{ K}$  [43]. The time step was set to 0.5 fs. Firstly the system was equilibrated at 300 K for 25 ps. Then the system was rapidly heated linearly with a rate of  $2 \times 10^{13} \text{ K/s}$ . Simulation parameters during implantation and crystallization are listed in Table 1.

### 3. Results and discussion

#### 3.1. $\text{Ga}^+$ FIB-induced damage

##### 3.1.1. Analysis approach

The evolution of system potential energy ( $E_p$ ), system total energy and system temperature after single Ga ion implanted is shown in Fig. 2a. System total energy equals to a sum of system potential energy and system kinetic energy. At the beginning of ion implantation, time step was set to a small value to adapt to the fast movement of atoms. During this period, system total energy kept stable, i.e., the temperature dissipation could be almost ignored. At the first 2000 interactions, the system temperature curve elevated and decreased rapidly forming a narrow peak. Meanwhile, the system potential curve was rising to peak value. The peak value of system potential energy was only 65% of the ion energy after the first ion energy implanted. In this process, gallium ions implanted into the silicon causing collision cascades. After the collision cascades, the system temperature slowly reduced to  $\sim 283 \text{ K}$  due to the temperature dissipation of Berendsen layer. System total energy and system potential energy also gradually reduced, but remained increase after per ion implanted due to the transformation from crystal phase to amorphous phase as a result of collision cascades.

The snapshot of sputtering system with various ion doses and various ion energies during impaction is shown in Figs. 3 and 4, respectively. (1 1 0) side views exhibit the vertical damage of FIB milling; and (0 0 1) top views reveal the lateral damage of FIB milling. The  $a\text{-Si}/c\text{-Si}$  interface is roughness because of the channelling effects. Due to the existence of Berendsen layer around the system and the smaller implantation area compared to the size of the simulation box, some silicon atoms along the border of the system is not disordered.

##### 3.1.2. FIB induced surface damage

To investigate surface deformation during 1 keV FIB milling, radial distribution function (RDF), bond length distribution, and bond angle distribution of the central surface are calculated as shown in Fig. 5. The atoms outside the blue box in Fig. 4b were

removed to calculate those values. And only atoms within the blue box contributed to the RDF, bond length distribution and bond angle distribution, i.e., the influence of atoms outside the blue box to the atoms near the edge of the box was eliminated. After FIB milling with the ion dose of  $2.0 \times 10^{14} \text{ cm}^{-2}$  (200 impacts), the Si atoms in the surface turned to long-range disordered (Fig. 5a). Before FIB milling, the peak value of Si–Si bond length is  $2.355 \text{ \AA}$ , closed to the bond length of  $c\text{-Si}$  of  $2.35 \text{ \AA}$  [44]. The peak value of bond length positively shifts and increases to  $2.365$  (10 impacts),  $2.365$  (50 impacts),  $2.405$  (200 impacts). The presence of bond angle distortion also implies an increase of defect concentrations in the structure (Fig. 5c).

To identify the defects in non-centre-symmetrical lattice, e.g. diamond lattice, common neighbour analysis (CNA) is employed for structure analysis [45]. The CNA is based on the topology of bonds that connect the surrounding neighbour atoms. The evolution of the defect region and sputtering yield with ion doses is shown in Fig. 6. The evolution of the defect region exhibits similar trends to the curve of system potential energy (Fig. 2b). The damage region increased rapidly, then turn to almost steady after a certain number of impacts. This evolution was also found in the formation of continued amorphous layer by MD simulation [22,26] and measurement by Rutherford backscattering spectroscopy [46]. When the projections only generate isolated Frenkel (interstitial-vacancy) pair or small defect accumulations at low ion doses ( $< 2 \times 10^{13} \text{ cm}^{-2}$ ), the defects area increased linearly with ion doses [21]. However, the acceleration in defects growth at low ion dose during 100 keV ion implantation [46], was not observed in our study. We attribute the change of defect region to the formation of surface amorphous layer. When the ion doses were low, the collision was mostly between impinging Ga ions and  $c\text{-Si}$  atoms. As the ion doses raised, Ga ions firstly collided with amorphous Si ( $a\text{-Si}$ ) atoms, then attacked some  $c\text{-Si}$  atoms. The energy of Ga ions might be wasted in the collisions with the amorphous layer, when the bombardments only generate local thermal melting which dissipates shortly afterwards.

The sputtering yield also decreased due to the energy dissipation of the amorphous layer. The sputtering yield is initially high and decreases to a stable value shown in Fig. 6b. Due to the change of microstructure and microchemistry of target, the sputtering yield for low ion dose is hard to be calculated by the volume of implanted region according to MD simulation [26] or atomic forced microscopy (AFM) measurement [47]. A drop of sputtering yield was also observed through secondary-neutral mass spectrometry in experiment, when ion doses were lower than  $2 \times 10^{15} \text{ ions/cm}^2$  [48]. The sputtering yield from an undamaged surface was about twice as large as that from a damaged surface, which is in accord with the data in the previous study [48].

The concentration of defects region and Ga ions along the original direction of Ga beams ( $z$  axis), which were computed over the whole simulation domain, is shown in Fig. 7. A bin width of  $2.715 \text{ \AA}$ , twice of the distance between two atomic planes in the diamond crystallization lattice of (0 0 1) orientation, was used for calculating the histograms profiles. As the Si atoms at the pristine surface have broken bonds, the CNA for the initial structure (impacts = 0) was subtracted to remove the peak at the surface ( $z = 0 \text{ \AA}$ ). Both the depth and range of defect region raised with the increase of ion doses and ion energies, which could be obviously observed in Figs. 3 and 4. The peak of CNA defects is beyond the surface and nearly approached the peak of Ga concentration. This peak moves deep into Si substrate with the deepening of Ga ions. The damage of subsurface (near  $z = 5 \text{ \AA}$ ) is a little lower than the peak value. The concentration of implanted Ga ions for different ion energies is shown in Fig. 7b. When the ion energy was lower, Ga ions implanted shallower, which brought a higher impurity density in the surface.

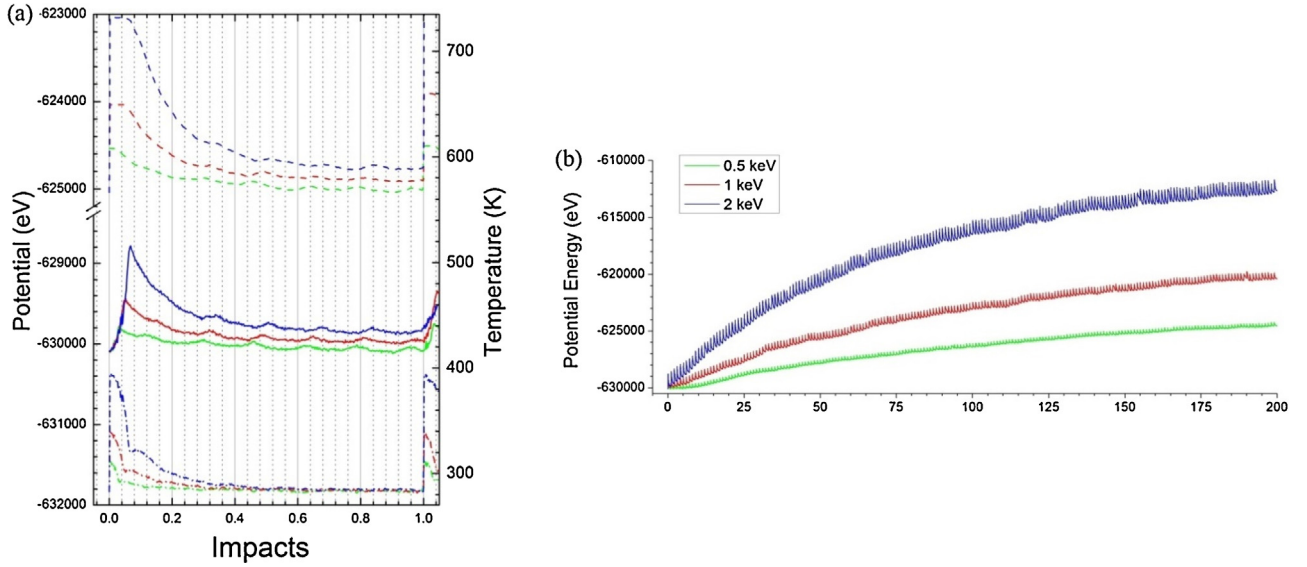


**Fig. 2.** System potential energy (line), system total energy (dash dot) and system temperature (dash) during the first Ga ion implantation (a). Potential energy (b) of the system as a function of ion doses for ion energies of 0.5 keV, 1 keV and 2 keV.

### 3.1.3. Evolution of surface topology during FIB milling

Surface topology for different ion doses and different ion energies is shown in the bottom of Fig. 8a–g. Atoms are coloured by z coordinates. Experimentally, ripples orientated parallel to the ion beam projection were observed after focused ion beam milling with small incident angle [49,50]. For the implantation of large cluster, due to the reduction in channelling effect, smooth hole with shallow ion implantation depth was obtained [23,24] and the sputtering yield was increased [24]. In our results, single ion impact caused a sharp pit at entry and swelling surrounded the pit. Si atoms in the surface were flowing during collision cascades, and the surface topology kept changing with ion doses. The formed pits would be covered by the new swelling.

Surface topology and vertical deviation of an ideal surface was described by root mean square (rms) roughness and surface average height ( $\bar{h}$ ) in our study. The definition of surface average height ( $\bar{h}$ )

and root mean square roughness for 2-dimension surface is given by

$$\bar{h} = \frac{1}{L^2} \sum_{i=1}^L \sum_{j=1}^L h_{ij} \quad (4)$$

$$\text{rms} = \left[ \frac{1}{L^2} \sum_{i=1}^L \sum_{j=1}^L (h_{ij} - \bar{h})^2 \right]^{1/2} \quad (5)$$

where  $h_{ij}$ ,  $i = 1, 2, \dots, L$ ;  $j = 1, 2, \dots, L$ , is the surface height at the  $i,j$ th position in the unit of layer,  $L$  presents the number of sampling.

When the ion doses are low, the irradiated surface was heightened, forming a swelling. Previous studies showed the measurement of the swelling caused by FIB fabrication with low ion

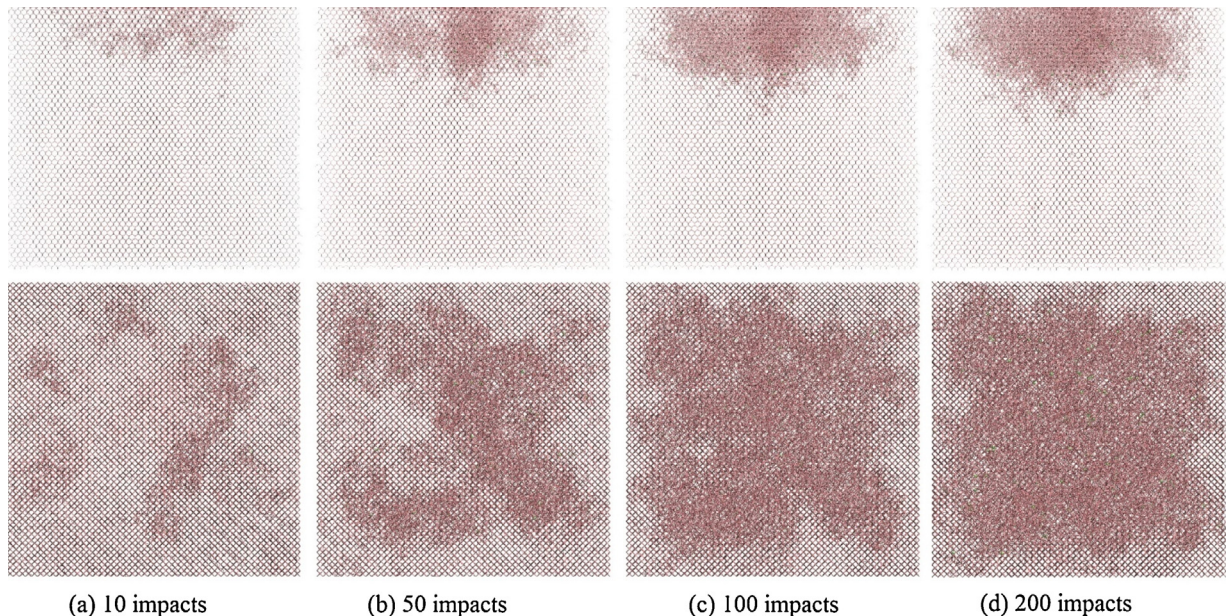


**Fig. 3.** Snapshots of the sputtering system after 1 keV Ga implantation with different ion doses: (a) 10 impacts ( $10 \times 10^{12} \text{ cm}^{-2}$  dose), (b) 50 impacts ( $50 \times 10^{12} \text{ cm}^{-2}$  dose), (c) 100 impacts ( $100 \times 10^{12} \text{ cm}^{-2}$  dose) and (d) 150 impacts ( $150 \times 10^{12} \text{ cm}^{-2}$  dose). (110) side views (top) and (001) top views (bottom) of the (001) oriented Si crystal.

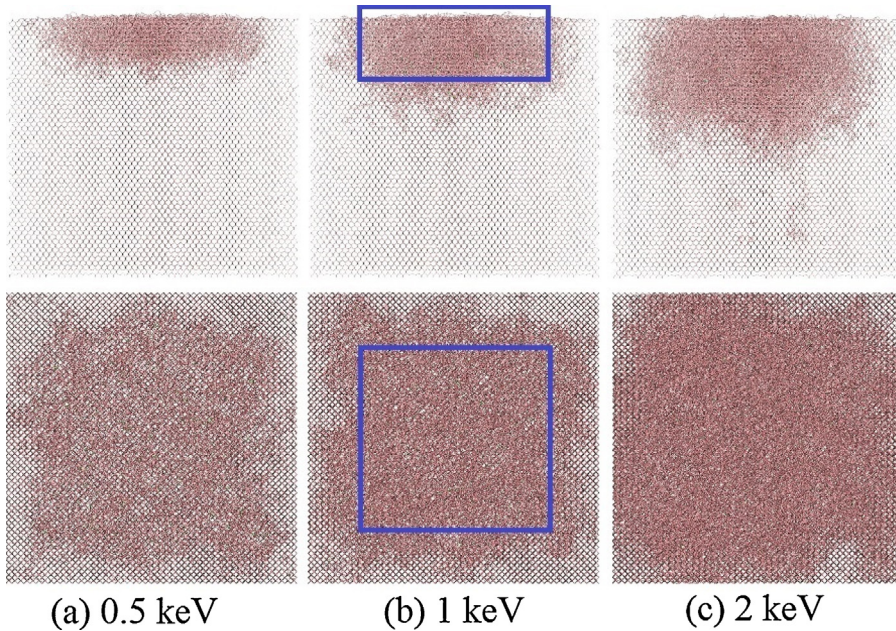


**Fig. 4.** Snapshots of the sputtering system after 200 impacts with different ion energies: 0.5 keV (a), 1 keV (b), 2 keV (c). (0 1 0) (top) and (1 1 0) (bottom) side views of the (0 0 1) oriented Si crystal after 200 impacts ( $2 \times 10^{14} \text{ cm}^{-2}$  dose). (d) Ga depth distribution in Si substrate for different ion energies.

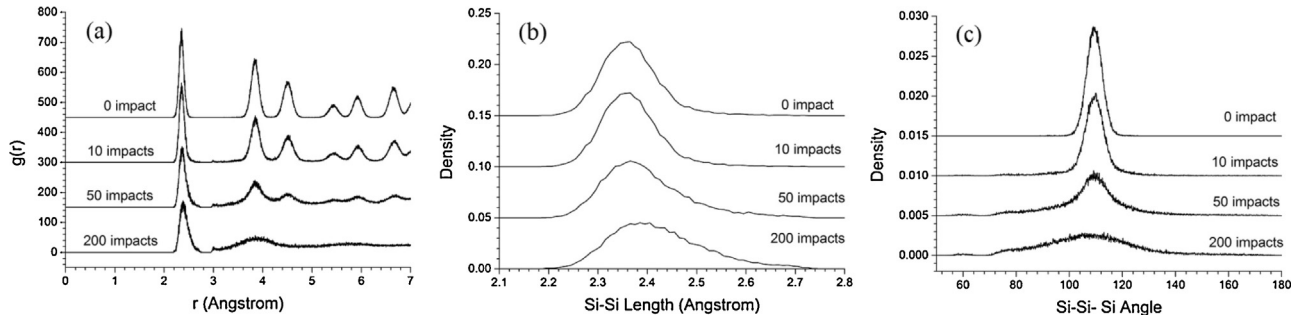


**Fig. 5.** Radial distribution function (a), Si–Si bond length distribution (b), and Si–Si–Si angle distribution (c) of the defect area for different ion doses. The defect area is  $80\text{\AA} \times 80\text{\AA} \times 30\text{\AA}$  at the upper middle of Si circled by blue box in Fig. 4b. (For interpretation of the references to colour in this figure legend, the reader is referred to the web version of the article.)

doses by AFM [13,47,51]. To obtain the surface topology after implantation, the scanning probe was simply regarded as a rigid cylinder bar with semi sphere at the end. Si atoms were regarded as rigid balls with the radius of  $1.175\text{\AA}$ . Scanning probes with the

radius of  $0.675\text{\AA}$ ,  $1.175\text{\AA}$ ,  $4.7\text{\AA}$ , and  $11.75\text{\AA}$  were used to measure the surface height, as shown in Fig. 9. Only the central surface with a size of  $24a_0 \times 24a_0$  ( $a_0 = 0.543\text{ nm}$ ) was calculated as shown in Fig. 8f. As the increase of the probe radius, the information of pits

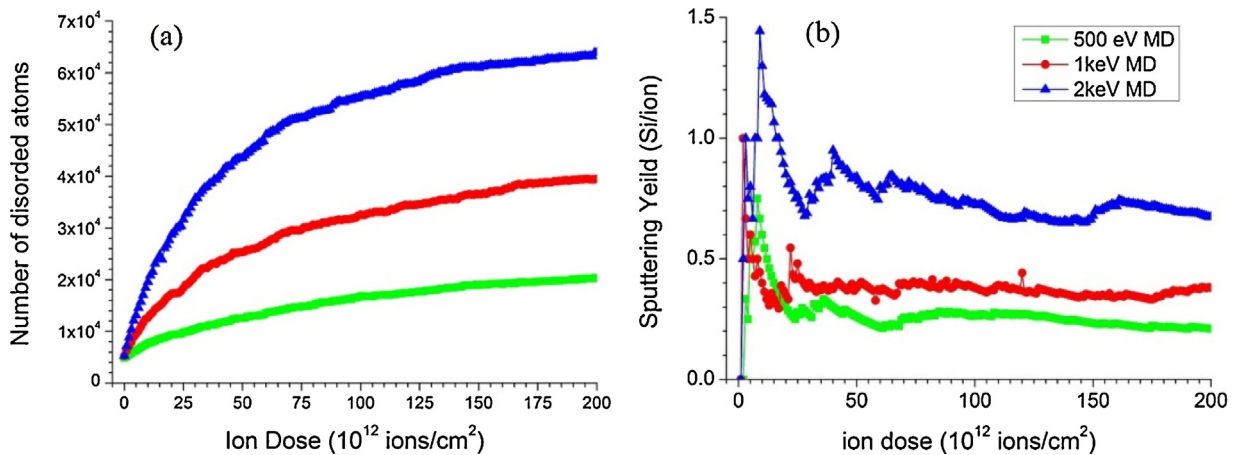


**Fig. 6.** The evolution of CNA damage area (a) and sputtering yield (b) as a function of ion doses.

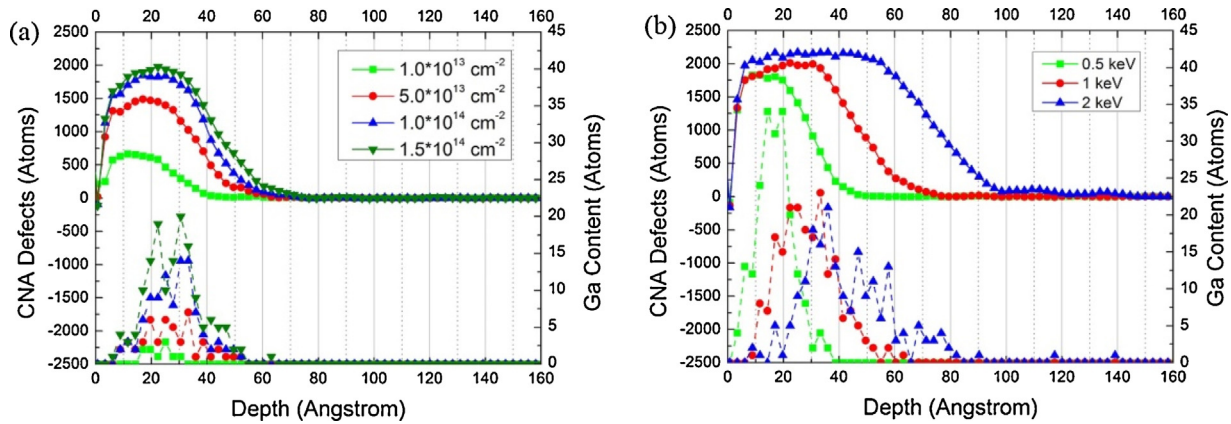


**Fig. 7.** The profiles of CNA damage area (line) and Ga depth distribution (dot) in Si substrate as shown in Figs. 3 and 4. (a) 1 keV Ga ions with different ion doses. (b) 0.5 keV, 1 keV and 2 keV Ga ions with the ion dose of  $2 \times 10^{14} \text{ cm}^{-2}$  (200 impacts). The initial surface at  $z = 0 \text{ \AA}$ .

was lost, leading to a rise of surface average height and a decrease of root mean square roughness.

Surface average height for different impacts is defined as  $H_i$ , where  $i$  is the total number of implanted Ga ions. Then, the height of undamaged surface should be  $H_0$ . And the swelling height relative to undamaged surface ( $H_s$ ) for different ion dose should be  $H_i - H_0$ . The swelling height and root mean square roughness was measured by probes with the radius of  $1.175 \text{ \AA}$  and  $11.75 \text{ \AA}$  as shown in Fig. 10. The Si substrate expanded as the amorphous area growth during FIB milling as shown in Fig. 6a. Both the height and the roughness of Si surface increased with ion doses. The ion implantation with higher ion energy also performed a greater surface average height. However, the evolution of RMS roughness was no striking difference among various ion energies. For various ion energies, the swelling heights calculated with a probe radius of  $11.75 \text{ \AA}$  are all greater than that of  $1.175 \text{ \AA}$ . And this disparity reached  $0.9 \text{ \AA}$  after 200 impacts.

Atomic density for different ion doses after 1 keV Ga ions implanted is shown in Fig. 11. The atomic densities of the

system are normalized by the Si density in the diamond cell crystal phase,  $0.0500 \text{ \AA}^{-3}$ . The increase of surface average height could be attributed to the decrease of density as a result of ion implantation. As atoms sputtering from the surface, the density of the top surface was reduced. Low density area, which indicated vacancies defects, would also be observed near the  $c\text{-Si}/a\text{-Si}$  interface, disagreeing with the result of Ar implantation with a flounce over  $10^{15} \text{ cm}^{-2}$  calculated by MEAM-L potential and SW potential [52]. TEM micrographs illustrated that interstitial type dislocation loops, named end-of-range (EOR), were formed just beneath the crystalline/amorphous interface by ion implantation in Si [53,54], which could also be observed in the MD simulation [25].

### 3.2. Annealing of the implantation area

#### 3.2.1. Annealing approach

After 1 keV  $\text{Ga}^+$  FIB implantation with 200 impacts, the system was annealed at 1400 K, 1600 K, 1800 K, 2000 K, 2200 K

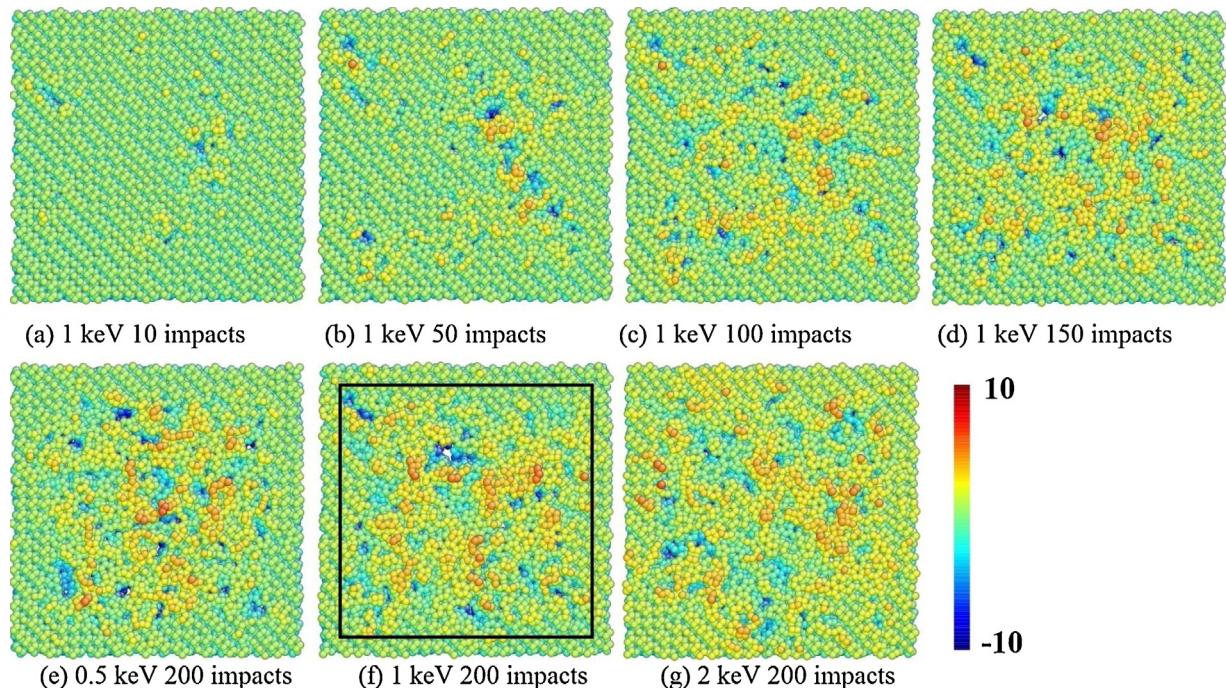


**Fig. 8.** The surface topography of the sputtering system (a-g). Coloured value based on the  $z$  coordinates of the atomic centre. The bar is from  $-10 \text{ \AA}$  to  $10 \text{ \AA}$ . (For interpretation of the references to colour in this figure legend, the reader is referred to the web version of the article.)

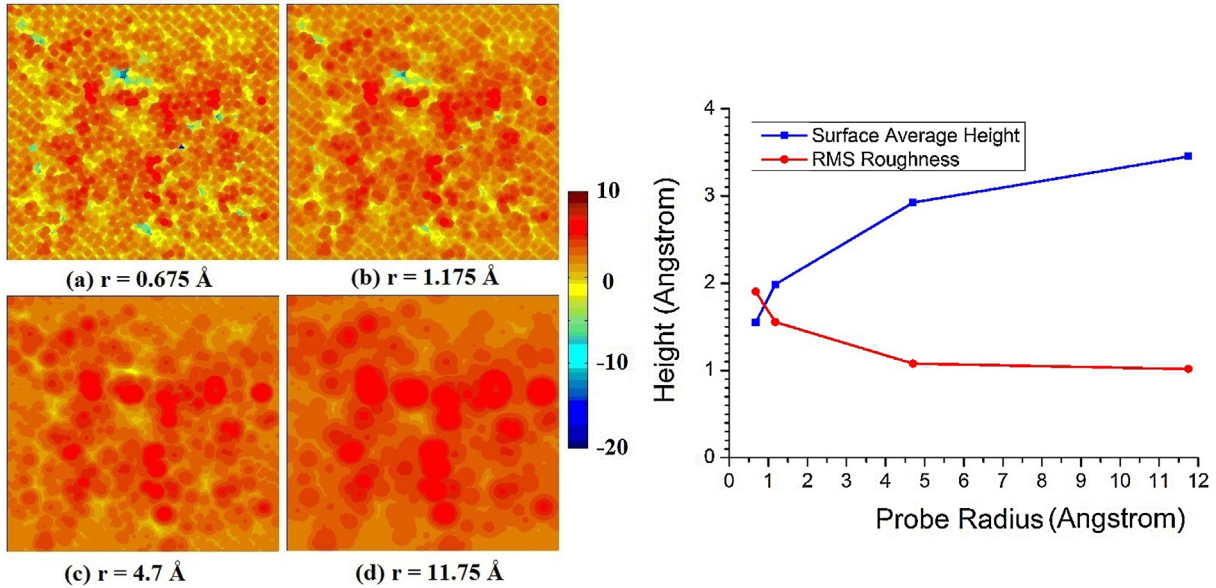


**Fig. 9.** The surface topography of the surface measured by different probe radii after 200 Ga ions implanted with energy of 1 keV. The Si atoms were assumed to be  $1.175 \text{ \AA}$ . Sampling density was  $0.025a_0 \times 0.025a_0$  ( $a_0 = 0.543 \text{ nm}$ ). Only the central surface with a size of  $22a_0 \times 22a_0$  was calculated as shown in Fig. 8f. Surface average height and root mean square roughness shown in the right.

( $= 0.863 \times T_{mc}$ ) and  $2400 \text{ K}$  ( $= 0.941 \times T_{mc}$ ), where  $T_{mc}$  is the melting point of crystalline silicon according to Tersoff-ZBL potential. According to Fig. 7b, few defects existed in the substrate deeper than  $65.16 \text{ \AA}$ . To save the source, Si atoms of low crystalline layer were deleted. When the system temperature raised in NPT ensemble, the simulation box expanded to keep a constant pressure, and the atomic separation resulted in an increase of potential energy. To exclude thermal effects, configurations extracted from the annealing process were cooled to  $2.5 \text{ K}$  instantly to calculate its properties.

The snapshots at the end of annealing at different temperatures are shown in Fig. 12. Obvious defects area could be observed in the central surface after 5 ns annealing below  $1800 \text{ K}$ . Some Ga ions still left inside the substrate as the temperature was lower than  $2000 \text{ K}$ . Few Ga ions left in the substrate after an annealing at  $2400 \text{ K}$  for  $2.4 \text{ ns}$ . As applied periodic boundary conditions at all six faces in annealing system, some precipitated Ga ions from the upper surface, went through the upper boundary and stucked on the lower surface. The process of annealing would be discussed in details in the next section.

**Fig. 13** displays the evolution of average potential energy per Si atom and the concentration of defect area as function of annealing time. During annealing, the amorphous phase relaxes and turns to crystalline phase, accompanying a decrease of the potential energy. When the temperature is less than  $2200 \text{ K}$ , the speed of crystallization is increased with annealing temperatures. The re-crystallization happened in  $1.1 \text{ ns}$  at  $2200 \text{ K}$ , as the slope of the potential energy turns to be zero after  $1.1 \text{ ns}$ . Most of the amorphous phase had been re-crystallized at  $2200 \text{ K}$  in  $1.1 \text{ ns}$ . The damage area fastly drops sharply from  $42.5\%$  to  $13\%$  in  $1.1 \text{ ns}$  at  $2200 \text{ K}$ . As the existence of broken bonds in upper and lower the surface, there would be even  $9.17\%$  defects in a perfect  $c\text{-Si}$  box calculating by means of CNA analysis. It is spent  $\sim 2.4 \text{ ns}$  to decline the concentration of disordered atoms to  $13\%$  as annealing at  $2000 \text{ K}$ . An annealing for  $5.0 \text{ ns}$  at  $1800 \text{ K}$  remains  $16.1\%$  disordered atoms. After  $5.0 \text{ ns}$  of annealing at  $1600 \text{ K}$  and  $1400 \text{ K}$  in, the defects were  $26.2\%$  and  $32\%$ , respectively, but the re-crystallization was still moving on extremely sluggishly. Some defects stuck around the Ga atoms or near the surface as annealed at  $2200 \text{ K}$  in  $2.0 \text{ ns}$  as shown in Fig. 12e. The crystallization

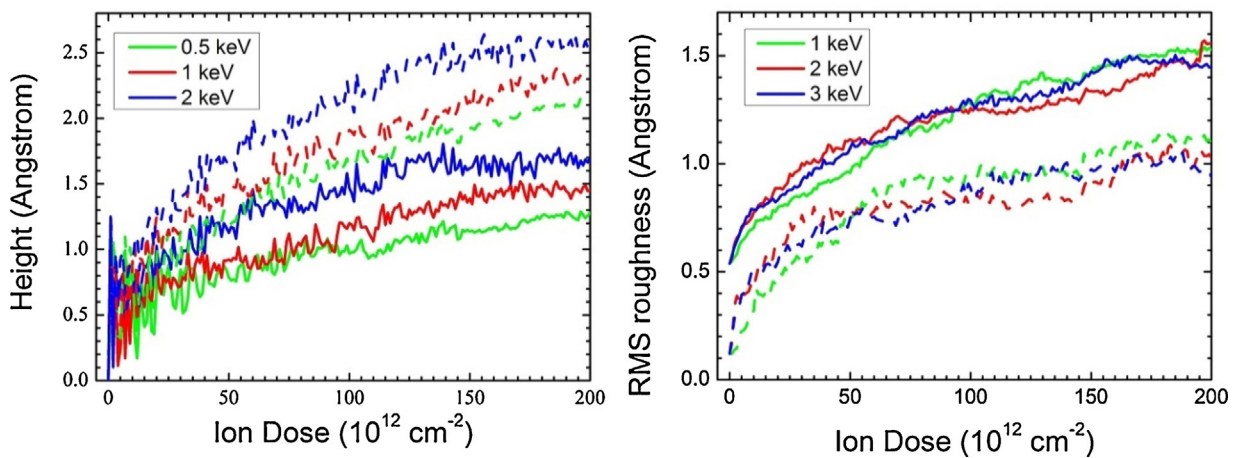


**Fig. 10.** Swelling height relative to undamaged surface (left) and root mean square roughness (right) during FIB milling. Probe radii of  $1.175 \text{ \AA}$  (line) and  $11.75 \text{ \AA}$  (dash) were calculated for different ion energies.

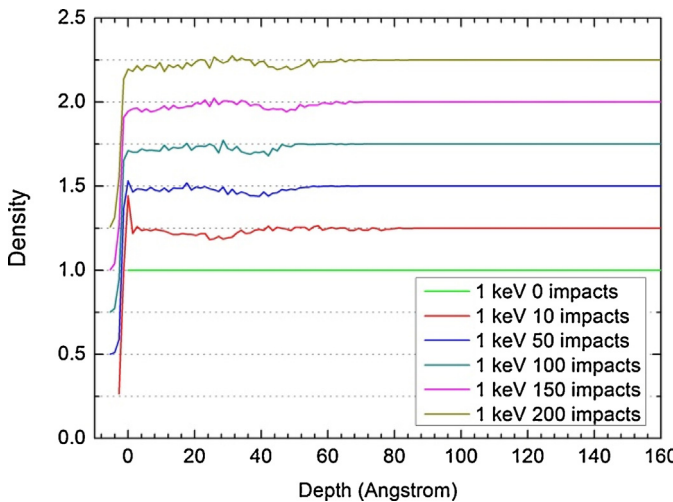


**Fig. 11.** Densities for different ion doses implanted by 1 keV Ga ion. Densities were stacked lined by +0.25 for various ion doses.

of *a*-Si was slower at 2400 K compared with 2200 K. The potential energy was elevated at the initial 0.5 ns annealing at 2400 K in 0.5 ns, which phenomenon can not be found in the evolution of CNA defects. The average potential energy of Si at the end of annealing at 2400 K was  $\sim 0.2$  eV higher than  $E_p$  at the end of annealing at 2200 K,

and the surface was still amorphous at 2400 K (Fig. 12f). Far from melting point, recrystallization velocity is determined by transport of Si to the interface which becomes faster with increasing temperature. Near melting point, recrystallization velocity is roughly proportional to  $T_m - T$ , where  $T_m$  is the melting temperature and  $T$  the system temperature [55].

### 3.2.2. System relaxation during annealing at 2200 K

The evolution of average potential energy per Si atom (a) and the defects concentration during annealing below 2200 K only exhibits the difference in the speed of re-crystallization. The process of re-crystallization at 2200 K is shown in Fig. 14. At the beginning of the annealing, the rough *a*-Si/c-Si interface (Figs. 14a and 16a) turn to smooth (Figs. 14c and 16c), and the amorphous pocket at the end of the collision had re-crystallized. Then, both *a*-Si at the sides and *a*-Si at the bottom of damage area turn to *c*-Si. Finally, the *a*-Si disappeared at the surface. Some defects still remained at the small isolated defects accumulation away from the continued amorphous zone, or around the Ga ions inside re-crystallized Si at the end of annealing. Caturla et al. has pointed out that small amorphous zone can be metastability against recrystallization during annealing [21]. And point defects outside the initial amorphous zone would remain after annealing [56]. Accumulation of Ga ions formed during annealing. A cluster with 28 Ga ions could be observed at the depth of 12 Å after annealing for 2.0 ns at 2200 K (Fig. 14h). During annealing, the characterization

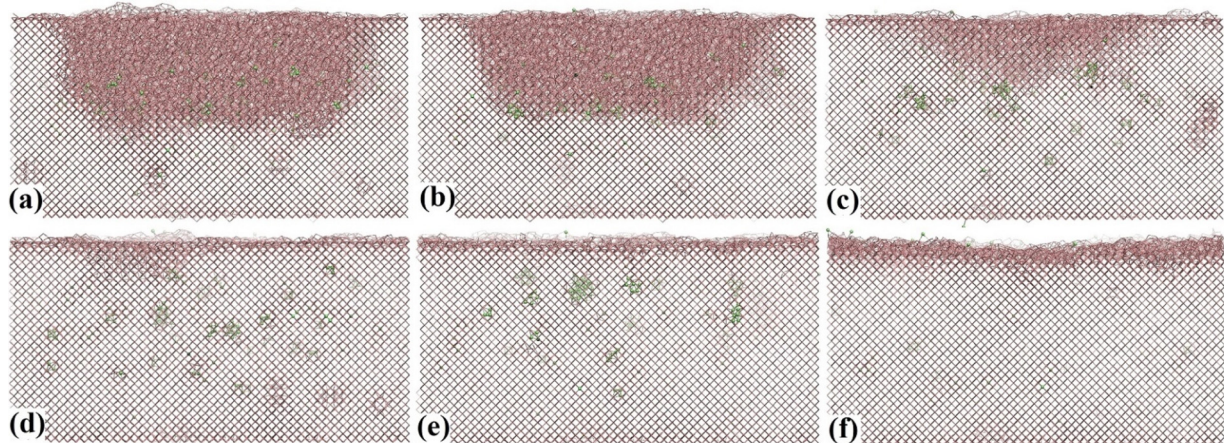


**Fig. 12.** (0 1 0) side views for different annealing temperature: (a) 10 ns at 1400 K; (b) 5 ns at 1600 K; (c) 5 ns at 1800 K; (d) 2.9 ns at 2000 K, (e) 2.0 ns at 2200 K, and (f) 2.4 ns at 2400 K. The green balls indicate Ga ions. (For interpretation of the references to colour in this figure legend, the reader is referred to the web version of the article.)

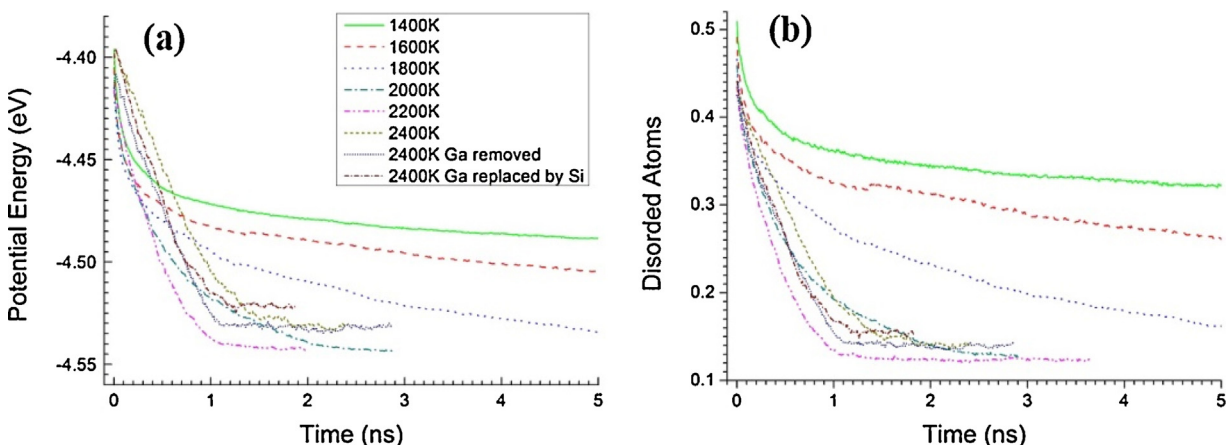


**Fig. 13.** The evolution of average potential energy per Si atom (a) and the defects concentration for different annealing temperatures.

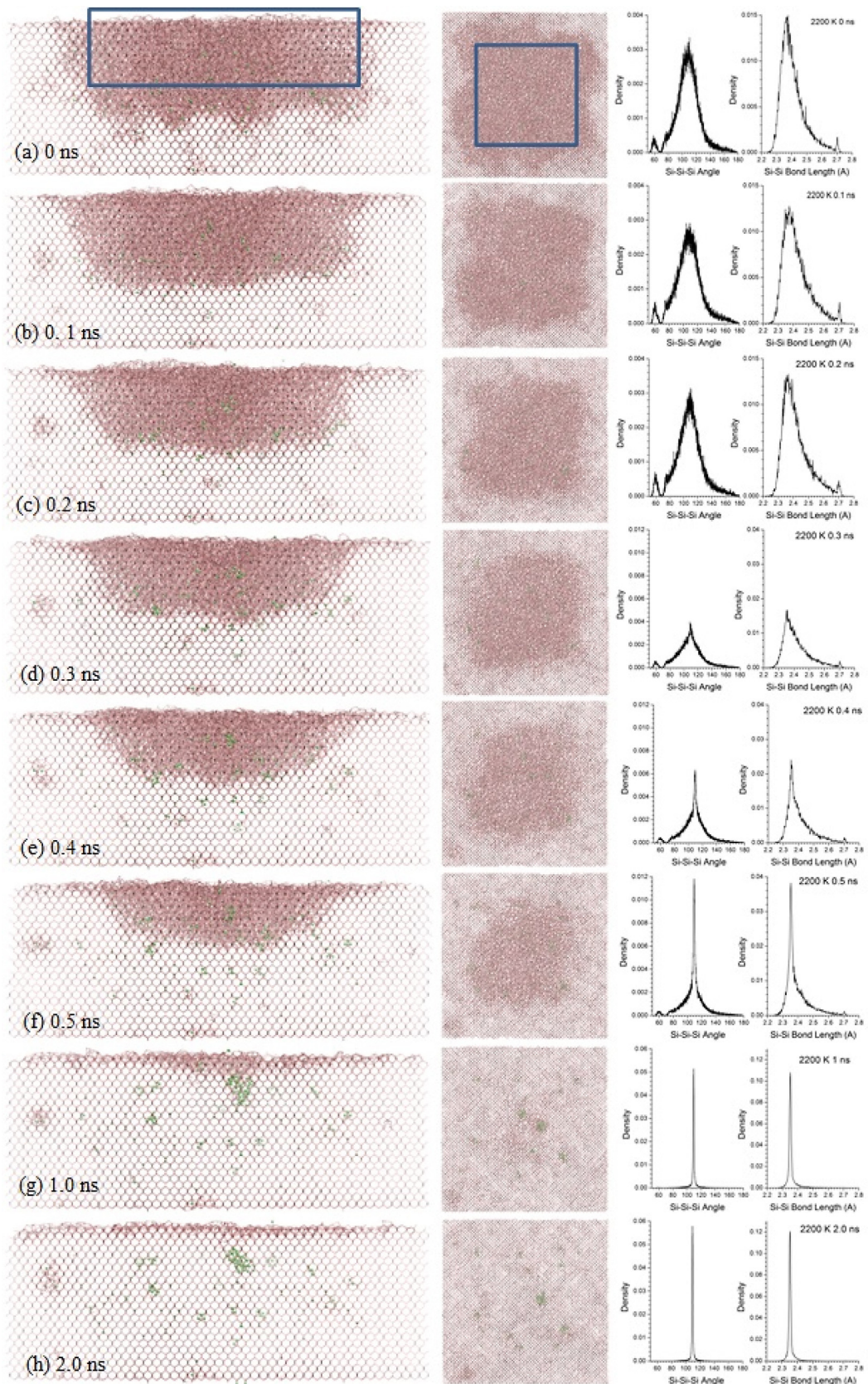


**Fig. 14.** (110) side views (left) and (010) side views (middle) of annealing at 2200 K. The green balls indicate Ga ions. Si—Si—Si bond angle and Si—Si—Si bond length of the calculated area are shown at the right of the snapshot. The size of the calculated area is  $80\text{ \AA} \times 80\text{ \AA} \times 30\text{ \AA}$  at the upper middle of Si circled by blue box as shown in Fig. 10a. (For interpretation of the references to colour in this figure legend, the reader is referred to the web version of the article.)

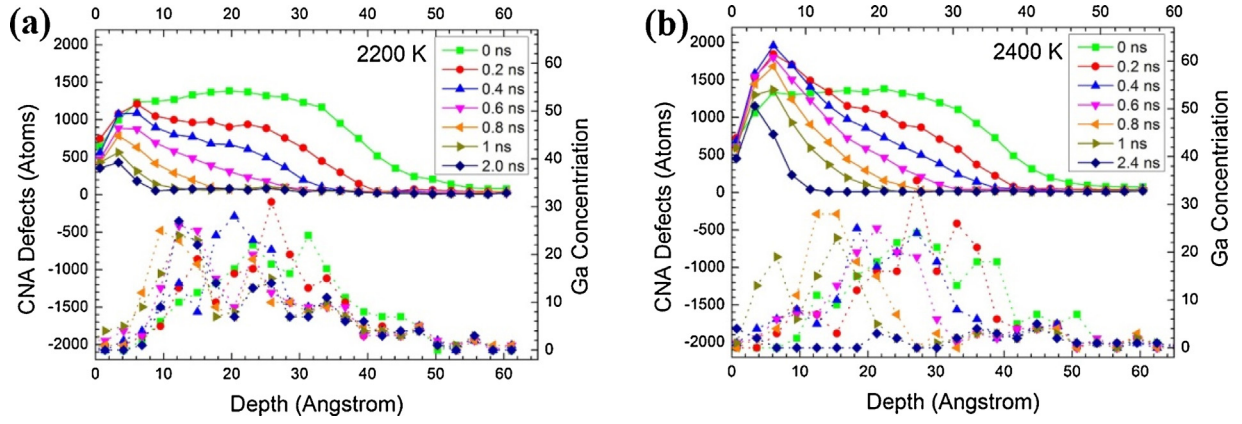


**Fig. 15.** The profiles of CNA damage area (line) and Ga depth distribution (dot) in Si substrate at 2200 K (a) and 2400 K (b).

of *a*-Si in the bond-angle distribution and bond-length distribution gradually decreased and finally disappeared. But the peak value near 109.5° of bond-angle distribution and peak value near 2.35 Å of bond-length distribution at 0.1 ns were abnormal decreased slightly.

Defects depth concentration for different annealing time in Fig. 15 also shows a re-crystallization process towards surface. The CNA defect of each layer beyond the surface decreases combining with the disappearance of *a*-Si at the bottom of the defect region in Fig. 15. Below the melting point of monocrystalline silicon (~2550 K), the amorphous material at the *a*-Si/*c*-Si interface gradually transformed into a crystal. As the *c*-Si is around the *a*-Si, the recrystallization process both towards the surface and towards the centre of the damage area.

### 3.2.3. System relaxation during annealing at 2400 K

The potential energy was elevated at the initial 0.5 ns annealing at 2400 K ( $= 0.941 \times T_{mc}$ ) as shown in Fig. 13. Fig. 14 shows the snapshots of annealing system at 2400 K. Contrary to the recrystallization at the bottom of *a*-Si, the *c*-Si around implantation damage area at the surface with a depth of  $\sim 15$  Å turns to amorphous phase (Fig. 16e). The defect concentration in the surface was heightened at the initially 0.4 ns during annealing at 2400 K as shown in Fig. 15b. The surface with a depth of about 5 Å was still amorphous at the end of annealing 2400 K shown in Figs. 15b and 16h. However, according to the evolution of CNA defects shown in Fig. 13b, the recrystallization process had stopped after 2.0 ns. According to experiment, the melting point of *a*-Si produced by  $^{28}\text{Si}$  ions implantation is 1480 K ( $= 0.878 \times T_{mc}^*$ ) compared to 1685 K for crystalline

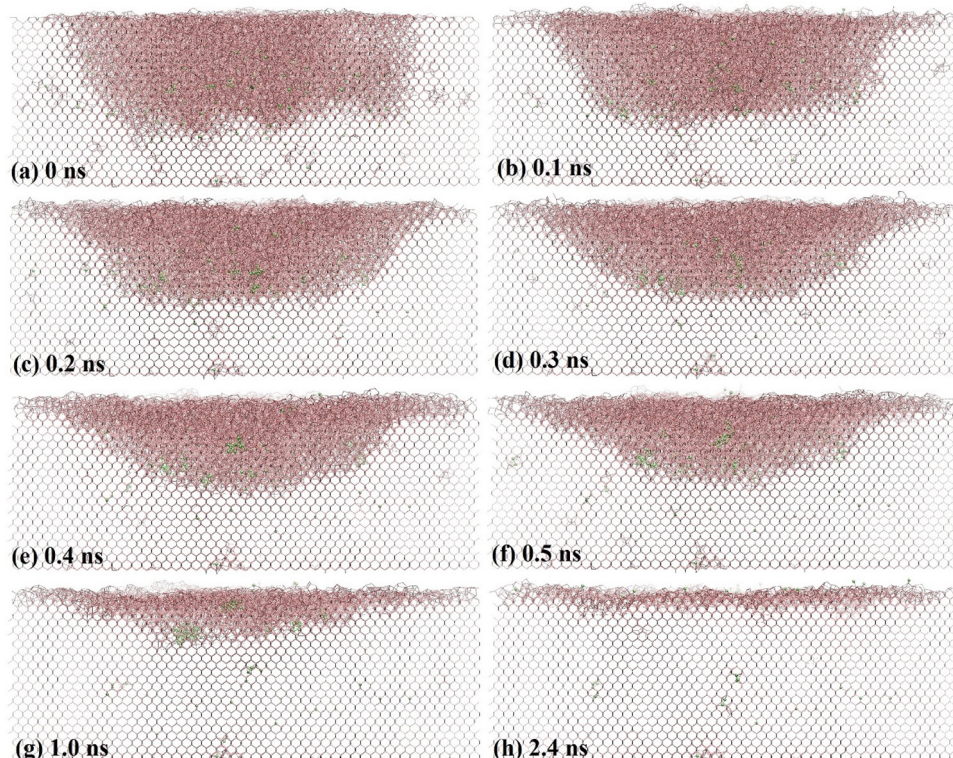


**Fig. 16.** (110) side views of the annealing system at 2400 K for different annealing times.

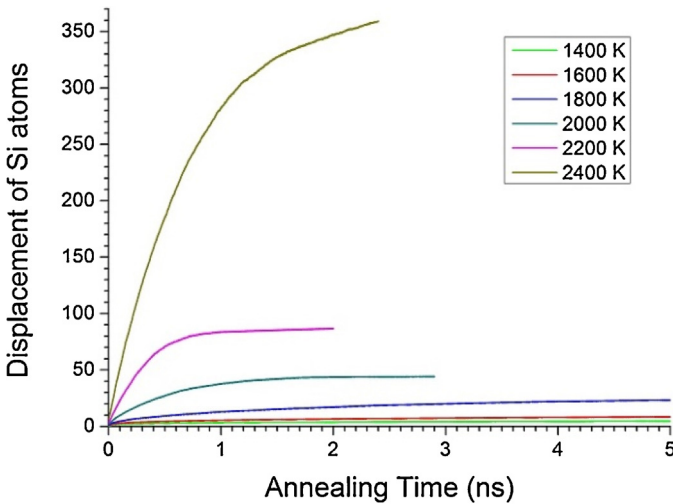


**Fig. 17.** Mean square displacement (MSD) of Si atoms for different annealing temperatures. The unit of average mean square displacement is Å.

Si [57]. However, the *a*-Si produced by As ions implantation melts at 1170 K ( $= 0.694 \times T_{mc}^*$ ) [58], as the sublimation point of solid arsenic is 887 K. As the system annealing at 2400 K after FIB milling, the Si atoms might melt from the surface to the inside body, while the *a*-Si at the *a*-Si/c-Si interface also transforms into a crystal at the bottom of *a*-Si area. To study the influence of Ga precipitation on recrystallization, the system with “zero Ga” was annealing at 2400 K. The mould, in which Ga atoms had been removed before annealing, and the mould, in which Ga atoms had been replaced by Si atoms, was both simulated respectively. The average potential energy and CNA defects in Fig. 13 illustrated that the recrystallization velocity increased without Ga precipitation. The surface melting phenomena was also observed and the potential energy is elevated. Besides, the Ga precipitation decreased recrystallization velocity to a certain degree.

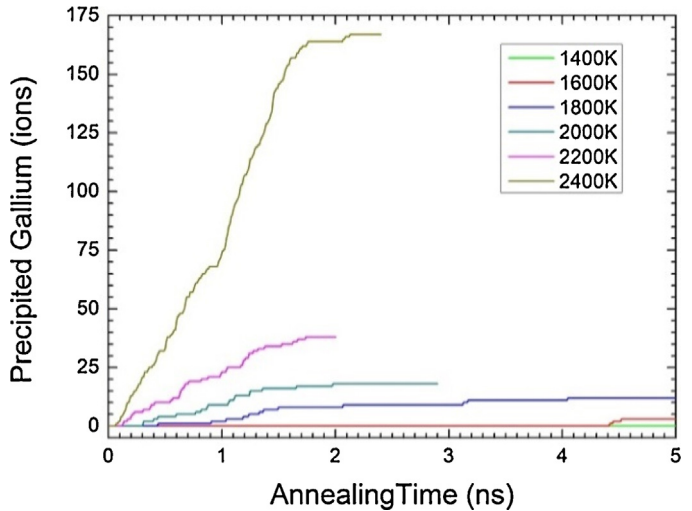


**Fig. 18.** The number of precipitated Ga ions at different annealing temperatures as a function of annealing time.

The mean square displacement of Si atoms was calculated to investigate the movement of Si atoms during annealing as shown in Fig. 17. The definition of the mean square displacement (msd) is given by:

$$\text{msd} = \frac{1}{N} \sum_{i=1}^N (dx_i^2 + dy_i^2 + dz_i^2) \quad (6)$$

where  $dx_i, dy_i, dz_i, i = 1, 2, \dots, N$ , is the displacement along  $x, y$  and  $z$  direction of the  $i$ th atom, respectively,  $N$  is the number of Si atoms.

As is known, there is an upper limited value of the mean square displacement for atoms in solid phase. In contrast, atoms in liquid phase and gas phase do not stay in the same place, but move about constantly. It could be observed that the mean square displacement changed with the alteration of CNA defect area in Fig. 13b, which indicated the re-crystallization process during annealing. Mean square displacement of Si atoms increased

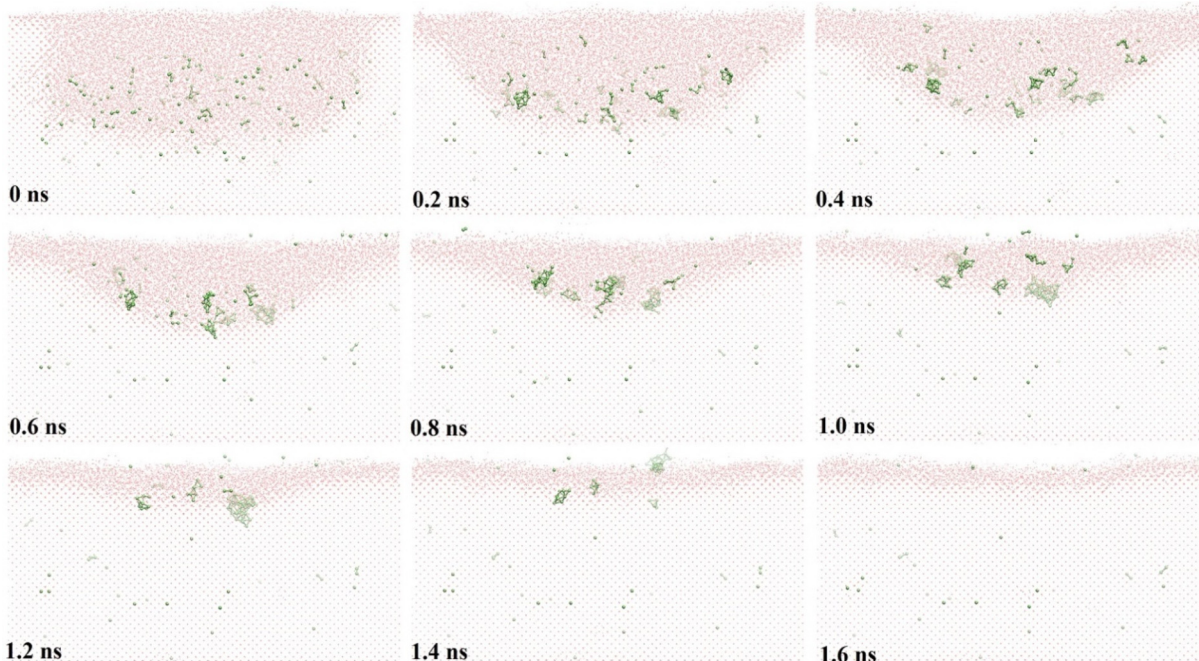


**Fig. 19.** The migration and precipitation of Ga ions as annealing at 2400 K. Pink point indicated Si. Green circle indicated Ga. Ga—Ga bonds with a distance shorter than 2.9 Å linked by green lines. (For interpretation of the references to colour in this figure legend, the reader is referred to the web version of the article.)

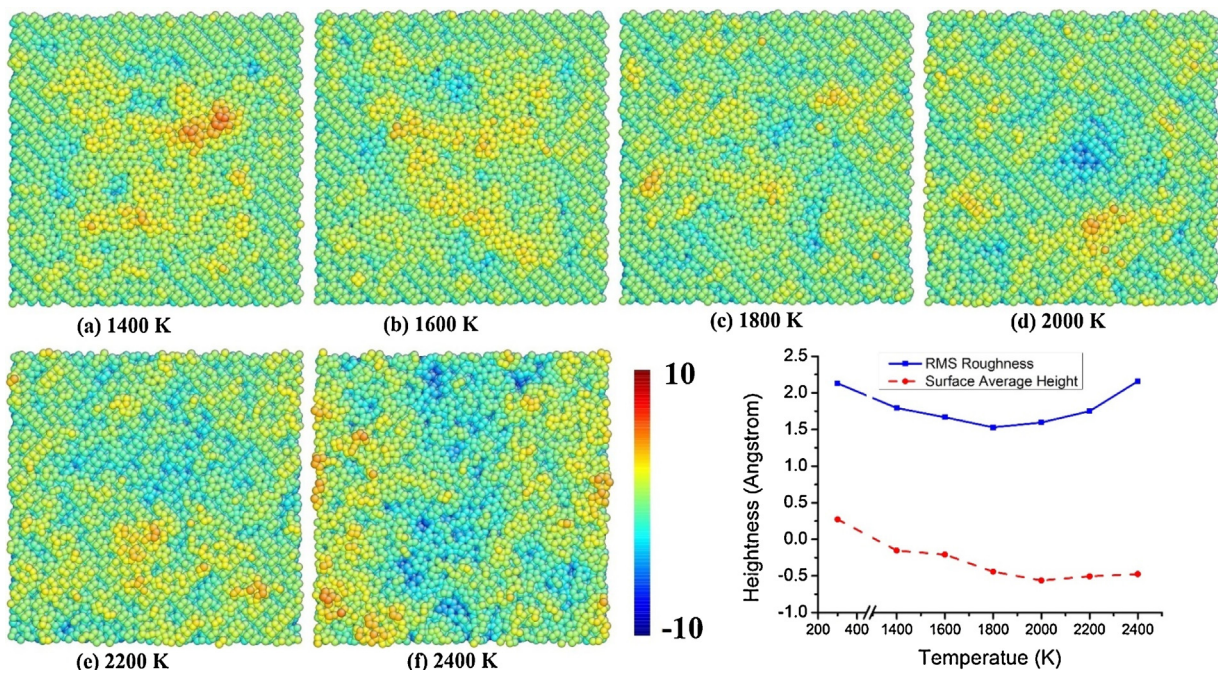


**Fig. 20.** Surface topography for different annealing temperatures at the end of annealing (a–f). Surface average height (ash) (dash) and root mean square (rms) roughness (line) at the end of annealing (g). The surface average height and root mean square roughness at 300 K was calculated by the value of the Si surface before annealing.

during the re-crystallization process, and kept unchanged after the re-crystallization of FIB damage area had stopped (2000 K, 2200 K). Mean square displacement of Si atoms grew slower as the speed of re-crystallization decreased. However, the mean square displacement for 2400 K still increased constantly even after the re-crystallization process stopped at 2.0 ns. That also proves our assumption of surface melting during annealing at 2400 K.

### 3.2.4. Migration and precipitation of Ga

In our previous work [29], the gallium have different level precipitation after annealing at different temperatures. In this simulation, Ga ions migrated together and were segregated from the Si substrate during annealing. The precipitated Ga ions were calculated and shown in Fig. 18. The Ga ions with a coordination number of zero were summed to the precipitated Ga ions. During the re-crystallization process of *a*-Si, the speed of precipitation grows with the raise of annealing temperatures in Fig. 18. The precipitation had stopped at the end of re-crystallization process.

For further study the influence of the re-crystallization process to the precipitation of Ga, the Ga depth distribution is also shown in Fig. 15. The peak of Ga concentration moved towards the surface with the *a*-Si/*c*-Si interface. ~80% Ga ions had remained in the *c*-Si after re-crystallization at 2200 K, while more than 75% Ga ions had precipitated after annealing at 2400 K.

The location of Ga ions for different annealing time as annealing at 2400 K is given in Fig. 19. The number of Ga–Ga bonds increased with the rise of annealing time, indicated an aggregation of Ga ions. The Ga clusters are located at the *a*-Si region near the *a*-Si/*c*-Si interface, leading to a moveable peak of Ga concentration with the interface as shown in Figs. 15 and 19. Dispersed Ga ions migrated together as *a*-Si/*c*-Si interface moving.

### 3.2.5. The evolution of surface topology during FIB milling

Surface topography for different temperatures is shown in Fig. 20. The radius of scanning probes was set to 1.54 Å. After annealing, Si atoms flowed to fill the pits caused by ion impacts in Fig. 8. Atoms at the swelling around the pits also flowed to the low-lying area. The surface became flat with the extent of re-crystallization

process as the temperature below 1800 K. When the temperature was higher than 1800 K, the surface average height decreased with the temperatures due to the precipitation of Ga ions shown in Fig. 18. Hollow region appeared in the central surface in Fig. 20d–f where a Ga cluster precipitated and left a hole at the end of annealing beyond 2000 K. Large sunken area was left in the centre as precipitated Ga ions increased at 2400 K.

## 4. Conclusion

In this paper, molecular dynamics simulations have been employed to study the dynamics of FIB-induced damage and subsequent annealing. Radial distribution function, bond length distribution, bond angle distribution, common neighbour analysis and root mean square roughness were calculated and analyzed. The experiment shows that:

Firstly, both the depth and range of the defect region raised with the increase of ion doses and ion energies. Continued amorphous layer was formed on the surface of implantation region after 1 keV Ga ion implantation with the ion dose of  $2.0 \times 10^{14}$  ions/cm<sup>2</sup> (200 impacts). The defect grew linearly at the beginning of ion implantation, when only point defects and dispersed amorphous pockets generated. Then the defects growth significantly slowed down before continued amorphous layer formed. The peak of defects is nearly approached the peak of Ga concentration.

Secondly, the swelling of implantation region result from the combination of surface roughening and the decrease in the surface density. Compared with virginal smooth surface, rough surface after FIB milling can lead to an increase of height in AFM measurement. Low density area, which is indicated vacancies defects, can be observed near the *c*-Si/*a*-Si interface.

Thirdly, the recrystallization lead to a *c*-Si regrowth processes both from the bottom towards the top surface and from periphery to centre. The profiles of CNA damage area represented a shortest recovery time of 2.0 ns at 2200 K. The recrystallization velocity was increased with annealing temperature far below the melting (<2000 K). Both melting on the top surface and recrystallization

at crystalline/amorphous interface have existed as annealing at 2400 K, which is near the melting point. Fourthly, Ga ions migrated together and were swept by the *c*-Si/*a*-Si interface during annealing. The content of precipitated Ga increased with temperature. The precipitation of Ga ions left sunken at the surface after annealed.

## Acknowledgements

The authors appreciate the support of the National Basic Research Program of China (973 Program, Grant No. 2011CB706700), National Natural Science Foundation of China (No. 51275559, 51320105009 and 90923038), National Science and Technology Major Project of China (2011ZX04014-071), and the “111” project by the State Administration of Foreign Experts Affairs and the Ministry of Education of China (Grant No. B07014).

## References

- [1] J. Mayer, L.A. Giannuzzi, T. Kamino, J. Michael, TEM sample preparation and FIB-induced damage, *MRS Bull.* 32 (2007) 400–407.
- [2] A. Lei, D.H. Petersen, T.J. Booth, L.V. Homann, C. Kallesoe, O.S. Sukas, Y. Gyrsting, K. Molhave, P. Boggild, Customizable *in situ* TEM devices fabricated in free-standing membranes by focused ion beam milling, *Nanotechnology* 21 (2010).
- [3] K. Lepinay, F. Lorut, Three-dimensional semiconductor device investigation using focused ion beam and scanning electron microscopy imaging (FIB/SEM tomography), *Microsc. Microanal.* 19 (2013) 85–92.
- [4] W.X. Li, C.Z. Gu, A.J. Cui, J.C. Fenton, Q.Q. Jiang, P.A. Warburton, T.H.H. Shen, Three-dimensional nanostructures by focused ion beam techniques: fabrication and characterization, *J. Mater. Res.* 28 (2013) 3063–3078.
- [5] Z. Liu, K. Iltanen, N. Chekurov, K. Grigoras, I. Tittonen, Aluminum oxide mask fabrication by focused ion beam implantation combined with wet etching, *Nanotechnology* 24 (2013) 175304.
- [6] J. Llobet, M. Sansa, M. Gerboles, N. Mestres, J. Arbiol, X. Borrise, F. Perez-Murano, Enabling electromechanical transduction in silicon nanowire mechanical resonators fabricated by focused ion beam implantation, *Nanotechnology* 25 (2014).
- [7] G.T.T. Sheng, C.F. Hu, W.J. Choi, K.N. Tu, Y.Y. Bong, L. Nguyen, Tin whiskers studied by focused ion beam imaging and transmission electron microscopy, *J. Appl. Phys.* 92 (2002) 64–69.
- [8] M. Cantoni, L. Holzer, Advances in 3D focused ion beam tomography, *MRS Bull.* 39 (2014) 354–360.
- [9] V.E. Krohn, G.R. Ringo, Ion source of high brightness using liquid metal, *Appl. Phys. Lett.* 27 (1975) 479–481.
- [10] H. Preston-Thomas, The international temperature scale of 1990 (ITS-90), *Metrologia* 27 (1990) 107.
- [11] L.W. Swanson, G.A. Schwind, A.E. Bell, J.E. Brady, Emission characteristics of gallium and bismuth liquid metal field ion sources, *J. Vac. Sci. Technol.* 16 (1979) 1864–1867.
- [12] S. Libertino, A. La Magna, Damage formation and evolution in ion-implanted crystalline Si, in: H. Bernas (Ed.), *Materials Science with Ion Beams*, Springer, Berlin Heidelberg, 2010, pp. 147–212.
- [13] P. Roediger, H.D. Wanzenboeck, S. Waid, G. Hochleitner, E. Bertagnolli, Focused-ion-beam-inflicted surface amorphization and gallium implantation-new insights and removal by focused-electron-beam-induced etching, *Nanotechnology* 22 (2011).
- [14] J. Schrauwen, D. Van Thourhout, R. Baets, Iodine enhanced focused-ion-beam etching of silicon for photonic applications, *J. Appl. Phys.* 102 (2007) 103104.
- [15] J. Tian, W. Yan, Y. Liu, J. Luo, D. Zhang, Z. Li, M. Qiu, Optical quality improvement of Si photonic devices fabricated by focused-ion-beam milling, *J. Lightwave Technol.* 27 (2009) 4306–4310.
- [16] E. Bellini, A. Taurino, M. Catalano, M. Lomascolo, A. Passaseo, L. Vasanelli, The effects of the focus ion beam milling process on the optical properties of semiconductor nanostructures, *Nanotechnology* 20 (2009).
- [17] A. Stanishevsky, B. Nagaraj, J. Melngailis, R. Ramesh, L. Khriachtchev, E. McDaniel, Radiation damage and its recovery in focused ion beam fabricated ferroelectric capacitors, *J. Appl. Phys.* 92 (2002) 3275–3278.
- [18] D. Cooper, A.C. Twitchett, P.K. Somodi, P.A. Midgley, R.E. Dunin-Borkowski, I. Farrer, D.A. Ritchie, Improvement in electron holographic phase images of focused-ion-beam-milled GaAs and Si p-n junctions by *in situ* annealing, *Appl. Phys. Lett.* 88 (2006) 063510.
- [19] T. Fujii, T. Namazu, K. Sudoh, S. Sakakihara, S. Inoue, Focused ion beam induced surface damage effect on the mechanical properties of silicon nanowires, *J. Eng. Mater. Technol.* 135 (2013) 041002.
- [20] N.I. Kato, Reducing focused ion beam damage to transmission electron microscopy samples, *J. Electron Microsc.* 53 (2004) 451–458.
- [21] M.J. Caturla, T. Díaz de la Rubia, L.A. Marqués, G.H. Gilmer, Ion-beam processing of silicon at keV energies: a molecular-dynamics study, *Phys. Rev. B* 54 (1996) 16683–16695.
- [22] J.A.V. Pomoell, A.V. Krasheninnikov, K. Nordlund, J. Keinonen, Ion ranges and irradiation-induced defects in multiwalled carbon nanotubes, *J. Appl. Phys.* 96 (2004) 2864–2871.
- [23] S. Ihara, S. Itoh, J. Kitakami, Mechanisms of cluster implantation in silicon: a molecular-dynamics study, *Phys. Rev. B* 58 (1998) 10736–10744.
- [24] T. Aoki, J. Matsuo, G. Takaoka, Molecular dynamics study of damage formation characteristics by large cluster ion impacts, *Nucl. Instrum. Methods Phys. Res. Sect. B: Beam Interact. Mater. Atoms* 202 (2003) 278–282.
- [25] M.F. Russo Jr., M. Maazouz, L.A. Giannuzzi, C. Chandler, M. Utlauf, B.J. Garrison, Trench formation and lateral damage induced by gallium milling of silicon, *Appl. Surf. Sci.* 255 (2008) 828–830.
- [26] L. Pastewka, R. Salzer, A. Graff, F. Altmann, M. Moseler, Surface amorphization, sputter rate, and intrinsic stresses of silicon during low energy Ga<sup>+</sup> focused-ion beam milling, *Nucl. Instrum. Methods Phys. Res. Sect. B: Beam Interact. Mater. Atoms* 267 (2009) 3072–3075.
- [27] A. Pan, Y.L. Wang, C.S. Wu, C.D. Chen, N.W. Liu, Effects of focused gallium ion-beam implantation on properties of nanochannels on silicon-on-insulator substrates, *J. Vac. Sci. Technol. B: Microelectron. Nanometer Struct.* 23 (2005) 2288–2291.
- [28] J.Y. Fang, S.Q. Qin, X.A. Zhang, D.Q. Liu, S.L. Chang, Annealing effect of platinum-incorporated nanowires created by focused ion/electron-beam-induced deposition, *Chin. Phys. B* 23 (2014).
- [29] Y.J. Xiao, F.Z. Fang, Z.W. Xu, W. Wu, X.C. Shen, The study of Ga<sup>+</sup> FIB implanting crystal silicon and subsequent annealing, *Nucl. Instrum. Methods Phys. Res. Sect. B: Beam Interact. Mater. Atoms* 307 (2013) 253–256.
- [30] A. Portavoce, M. Kammler, R. Hull, M.C. Reuter, F.M. Ross, Mechanism of the nanoscale localization of Ge quantum dot nucleation on focused ion beam templated Si(001) surfaces, *Nanotechnology* 17 (2006) 4451–4455.
- [31] J.Y. Lee, M.J. Noordhoek, P. Smereka, H. McKay, J.M. Millunchick, Filling of hole arrays with InAs quantum dots, *Nanotechnology* 20 (2009) 285305.
- [32] A. Portavoce, R. Hull, M.C. Reuter, F.M. Ross, Nanometer-scale control of single quantum dot nucleation through focused ion-beam implantation, *Phys. Rev. B* 76 (2007).
- [33] H.J.C. Berendsen, J.P.M. Postma, W.F. van Gunsteren, A. DiNola, J.R. Haak, Molecular dynamics with coupling to an external bath, *J. Chem. Phys.* 81 (1984) 3684–3690.
- [34] E.F.C. Haddeman, B.J. Thijssse, Transient sputtering of silicon by argon studied by molecular dynamics simulations, *Nucl. Instrum. Methods Phys. Res. Sect. B: Beam Interact. Mater. Atoms* 202 (2003) 161–167.
- [35] S. Plimpton, Fast parallel algorithms for short-range molecular dynamics, *J. Comput. Phys.* 117 (1995) 1–19.
- [36] W. Humphrey, A. Dalke, K. Schulten, VMD: visual molecular dynamics, *J. Mol. Graph.* 14 (1996) 33–38.
- [37] J. Li, AtomEye: an efficient atomistic configuration viewer, *Modell. Simul. Mater. Sci. Eng.* 11 (2003) 173–177.
- [38] J. Ziegler, J. Biersack, U. Littmark, *The Stopping and Range of Ions in Solids*, Pergamon, New York, 1985.
- [39] J. Tersoff, Modeling solid-state chemistry: interatomic potential for multicomponent systems, *Phys. Rev. B* 39 (1989) 5566–5568.
- [40] M. Nakamura, H. Fujioka, K. Ono, M. Takeuchi, T. Mitsui, M. Oshima, Molecular dynamics simulation of III-V compound semiconductor growth with MBE, *J. Cryst. Growth* 209 (2000) 232–236.
- [41] S.J. Cook, P. Clancy, Comparison of semi-empirical potential functions for silicon and germanium, *Phys. Rev. B* 47 (1993) 7686–7699.
- [42] L. Pastewka, A. Klemenz, P. Gumbsch, M. Moseler, Screened empirical bond-order potentials for Si-C, *Phys. Rev. B* 87 (2013) 205410.
- [43] C.J. Glassbrenner, G.A. Slack, Thermal conductivity of silicon and germanium from 3 K to the melting point, *Phys. Rev.* 134 (1964) A1058–A1069.
- [44] L. Pelaz, L.A. Marqués, J. Barbolla, Ion-beam-induced amorphization and recrystallization in silicon, *J. Appl. Phys.* 96 (2004) 5947–5976.
- [45] J.D. Honeycutt, H.C. Andersen, Molecular dynamics study of melting and freezing of small Lennard-Jones clusters, *J. Phys. Chem.* 91 (1987) 4950–4963.
- [46] O.W. Holland, S.J. Pennycook, G.L. Albert, New model for damage accumulation in Si during self-ion irradiation, *Appl. Phys. Lett.* 55 (1989) 2503–2505.
- [47] L. Frey, C. Lehrer, H. Ryssel, Nanoscale effects in focused ion beam processing, *Appl. Phys. A: Mater. Sci. Process.* 76 (2003) 1017–1023.
- [48] J.W. Burnett, M.J. Pellin, W.F. Calaway, D.M. Gruen, J.T. Yates, Ion dose dependence of the sputtering yield of Ru(0001) at very low fluences, *Phys. Rev. Lett.* 63 (1989) 562–565.
- [49] B. Ziberi, F. Frost, T. Hoche, B. Rauschenbach, Ripple pattern formation on silicon surfaces by low-energy ion-beam erosion: experiment and theory, *Phys. Rev. B* 72 (2005).
- [50] S. Habenicht, K.P. Lieb, J. Koch, A.D. Wieck, Ripple propagation and velocity dispersion on ion-beam-eroded silicon surfaces, *Phys. Rev. B* 65 (2002).
- [51] B.D. Huey, R.M. Langford, Low-dose focused ion beam nanofabrication and characterization by atomic force microscopy, *Nanotechnology* 14 (2003) 409–412.
- [52] M. Timonova, B.J. Thijssse, Molecular dynamics simulations of the formation and crystallization of amorphous Si, *Comput. Mater. Sci.* 50 (2011) 2380–2390.
- [53] K.S. Jones, D. Venables, The effect of implant energy, dose, and dynamic annealing on end-of-range damage in Ge<sup>+</sup>-implanted silicon, *J. Appl. Phys.* 69 (1991) 2931–2937.
- [54] L.S. Robertson, K.S. Jones, L.M. Rubin, J. Jackson, Annealing kinetics of {311} defects and dislocation loops in the end-of-range damage region of ion implanted silicon, *J. Appl. Phys.* 87 (2000) 2910–2913.

- [55] M.D. Kluge, J.R. Ray, Velocity versus temperature relation for solidification and melting of silicon: a molecular-dynamics study, *Phys. Rev. B* 39 (1989) 1738–1746.
- [56] L.A. Marques, L. Pelaz, I. Santos, V.C. Venezia, Characterization of octadecaborane implantation into Si using molecular dynamics, *Phys. Rev. B* 74 (2006) 201201.
- [57] M.O. Thompson, G.J. Galvin, J.W. Mayer, P.S. Peercy, J.M. Poate, D.C. Jacobson, A.G. Cullis, N.G. Chew, Melting temperature and explosive crystallization of amorphous silicon during pulsed laser irradiation, *Phys. Rev. Lett.* 52 (1984) 2360–2363.
- [58] P. Baeri, G. Foti, J.M. Poate, A.G. Cullis, Phase transitions in amorphous Si produced by rapid heating, *Phys. Rev. Lett.* 45 (1980) 2036–2039.